Design and Evaluation of a Miniaturized Force Sensor Based on Wave Backscattering

Daegue Park, Agrim Gupta, Shayaun Bashar, Cédric Girerd, Dinesh Bharadia, and Tania. K. Morimoto, *Member, IEEE*

***Abstract*—The ability to sense forces is a critical component for ensuring that robots can safely interact with their environment. Yet there are numerous situations, in particular for medical applications, where environmental and sensor density requirements can pose challenges to sensor design. In our previous work, we presented a novel wireless force sensing paradigm based on wave backscattering. In this paper, we present an improved and miniaturized design suitable for wireless communications. We present an end-to-end simulation of the proposed sensor, its fabrication, modeling, and experimental validations in a wired setting. Our sensor can sense forces in the range of 0 to 6 N, with a Root Mean Square (RMS) error of 0.17 N, on average, for our two sensor prototypes, and it provides wireless compatibility in a range of frequencies adapted for use inside the human body. We present a demonstration of contact force sensing with our sensors mounted on the body of a continuum robot and show its potential to enable applications in fields such as medical robotics.**

***Index Terms*—Capacitive sensors, force sensors, medical robotics.**

I. Introduction

SENSORS are a critical component of robotic systems, necessary for ensuring safety and precision during the execution of complex tasks. As robots transition into operating in more constrained and sensitive environments, including inside the human body, force sensors in particular, become increasingly important. Force information can be used to help prevent damage to the surrounding environment [1], to improve robot control during delicate tasks [2], and even to estimate the deflection of the robot itself in the case of soft and flexible robots [3]. However, there are many scenarios where integration of existing force sensors becomes challenging to impossible based on incompatibility with the environment or because of their size, stiffness, or general form factor [4]. We focus here on the development of a new force sensor to overcome these challenges for applications in medical robotics, starting with applications in, for example, cardiothoracic, laparoscopic, and urologic procedures.

A. Force Sensors for Medical Robots

Force sensing is especially important for medical applications [5]. For example, for teleoperated surgical robots, real-time force measurements can provide surgeons with direct feedback on applied forces, rather than leaving them to rely on visual feedback alone [6]. Force information can therefore help to minimize damage to surrounding tissues by ensuring applied forces are limited to safe levels [7]. Several force sensing technologies have been proposed for medical applications (see [6] for a detailed review). Such sensors include, for example, strain gauges [8], piezoelectric [9], optical [10], magnetic [11], and capacitive [12] sensors. While these sensing technologies can provide high accuracy measurements with small form factors, they are usually wired, which poses integration issues for sensing forces along a 1-D or 2-D space.

Indeed, it can be important to measure forces applied along the entire length of a robot, particularly in the case of flexible, continuum robots [13]. The shape of these robots can be affected by loads induced during interaction with the environment, and the integration of sensors can help for improved shape estimation and control. While many types of sensors have been developed to measure or estimate the shape of continuum robots, including optical fibers, FBG and light intensity sensors, and electromagnetic and optical trackers [14], they usually provide an indirect and incomplete way of estimating forces. Indeed, solving for force magnitude and location from the observed deformed shape of robots has proved to have some critical limitations [15]. In particular, such methods have typically been limited to the case of only two applied forces, have proven to be sensitive to the robot stiffness and the accuracy of the tracking system used [15], and cannot be used to estimate antagonistic applied forces. Researchers have also proposed force sensors for flexible instruments and continuum robots and have integrated them on their bodies [16] in order to measure such information directly.

B. Miniaturized Wireless Force Sensors

Despite advancements in the development of force sensors for medical robots, there remain challenges with measuring forces

Manuscript received 24 February 2022; accepted 7 June 2022. Date of publication 20 June 2022; date of current version 28 June 2022. This letter was recommended for publication by Associate Editor M. Gauthier and Editor A. Banerjee upon evaluation of the reviewers' comments. This work was supported by National Science Foundation under Grant 1935329. *(Corresponding authors: Daegue Park; Cédric Girerd.)*

Daegue Park and Cédric Girerd are with the Department of Mechanical and Aerospace Engineering, University of California, San Diego, La Jolla, CA 92093 USA (e-mail: dpark025@gmail.com; cgirerd@eng.ucsd.edu).

Agrim Gupta, Shayaun Bashar, and Dinesh Bharadia are with the Department of Electrical and Computer Engineering, University of California, San Diego, La Jolla, CA 92093 USA (e-mail: agg003@eng.ucsd.edu; sbashar@ucsd.edu; dineshb@ucsd.edu).

Tania. K. Morimoto is with the Department of Mechanical and Aerospace Engineering and the Department of Surgery, University of California, San Diego, La Jolla, CA 92093 USA (e-mail: tkmorimoto@eng.ucsd.edu).

Digital Object Identifier 10.1109/LRA.2022.3184767

across the entire robot surface, particularly when space must be reserved for the passage of surgical instruments. Researchers have proposed a few main approaches for wireless force sensors that can help overcome these challenges. These approaches include LC resonant sensors [17], NFC-based sensors [9], and SAW-based strain sensors [18]. However, these sensors have very low interrogation distances and have not been shown to work reliably in a realistic environment where wireless signals undergo rich scattering effects [19].

While we proposed a sensor paradigm for wireless usage based on Radio Frequency (RF) backscattering [20], [21] to address these challenges for wireless force sensors, the associated mechanical architecture was not well-suited for miniaturization. It relied on a change in contact location between a signal and ground trace in order to change the total travel distance of a reflected electromagnetic wave as $\Delta S_{phase} = \gamma \Delta x$, where $\gamma = \frac{2\pi f}{c}$, Δx is the difference in travel distance of the wave, and f is the frequency of the wave. Because the maximum travel distance of the wave is directly related to the sensor length, decreasing the sensor length for miniaturization would result in a smaller range of S_{phase} and therefore lower sensing resolution [20]. While increasing the frequency could allow for smaller designs, there is an upper bound at 1 GHz [22] since higher frequencies cannot easily penetrate human tissue. The overall result of relying on changes in contact trace locations to induce phase change is that micro or millimeter-scale sensors would lead to only minimal phase shifts. To overcome this limitation, we propose a new, capacitor-like design, which relies on impedance change as a signal trace gets closer to a ground trace, rather than on a length change-induced phase change.

C. Contributions

The contributions of this work are as follows. First, we present a new type of sensor design that relies on the wave backscattering principle. It is different in its working mechanism compared to our previous work, as it is no longer based on a change in contact location between a signal and ground trace, which poses miniaturization issues. Instead, it is based on a change of impedance induced as the distance between such traces varies. Second, we propose a multiphysics model of the sensor that can be used to simulate its behavior, as design parameters are varied. Third, we use the developed multiphysics model to design and fabricate sensor prototypes. The sensors are designed to measure forces between 0 N to 6 N to accommodate various surgical procedures. Finally, we demonstrate the sensor's potential for measuring forces applied to the body of a continuum robot (see Fig. 1).

II. Sensor Modeling

In this section, we describe the sensor's working principle and propose an end-to-end simulation for design purposes.

A. Working Principle

The working principle relies on a change in capacitance, and therefore impedance, to convert an applied force into a phase shift. The sensor is composed of three layers: a conductive layer on the top and the bottom, and a soft polymer layer in between. The bottom conductive layer is connected to a signal trace, while the top one is grounded. The soft polymer layer effectively acts like a dielectric medium separating the conductive layers, similar to a parallel plate capacitor, as illustrated in Fig. 2. The initial capacitance of the sensor at steady-state is $C = \epsilon \frac{A}{d}$, where ϵ is the dielectric permittivity, A is the surface area of the conductive plates, and d is the distance between them. As a force is applied to the sensor, the soft polymer deforms and brings the conductive layers closer together, leading to an increase in the sensor capacitance. Hence, the sensor capacitance is a function of applied force, denoted as $C(F)$. From an RF perspective, this change in capacitance leads to a change in the sensor impedance, given by $Z = \frac{1}{j\omega C(F)}$, where $\omega = 2\pi f$, f is the wave frequency, and F is the force applied. This change in impedance results in a change in the phase of the wave, since $S_{phase} = 2\tan^{-1}(\frac{1}{50\omega C(F)})$. Therefore, the external force causes a phase difference between the transmitted and reflected wave, as illustrated in Fig. 2.

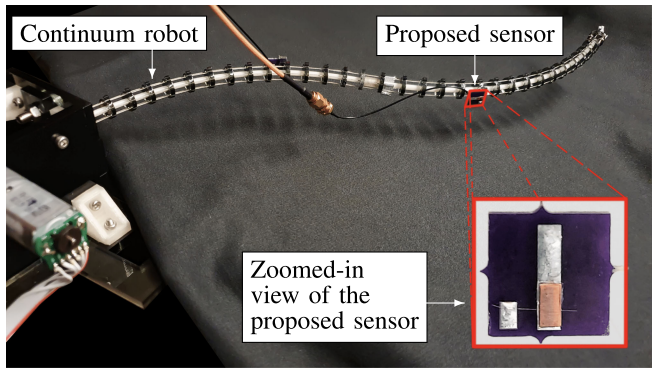

Fig. 1. Picture of the proposed force sensors assembled on a continuum robot, with a close-up view of the sensor in the bottom right corner.

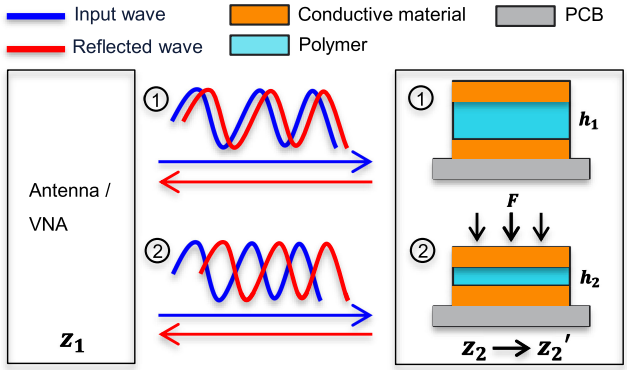

Fig. 2. Illustration of the working principle of the proposed sensor. As a force is applied, the soft polymer layer deforms and brings the conductive layers closer together, leading to a change in the impedance of the sensor, which results in a change in the phase of a reflected RF signal.

B. End-to-End Simulation

We created an end-to-end Finite Element Analysis (FEA) simulation that models both the mechanical and RF components of our sensor and that can be used to determine a set of sensor design parameters for a given application. To do so, we used

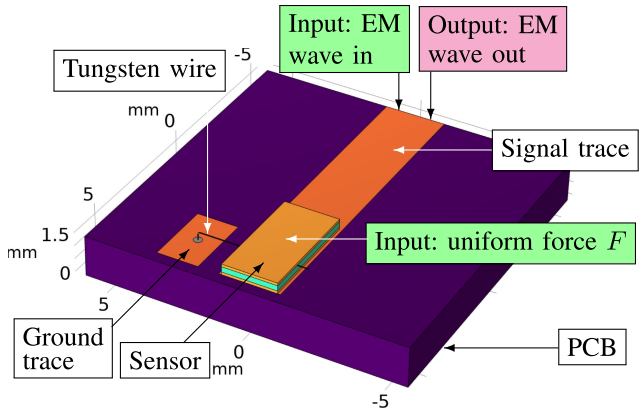

Fig. 3. Model of the sensor, PCB, signal trace, ground trace, and tungsten wire, as implemented in COMSOL Multiphysics.

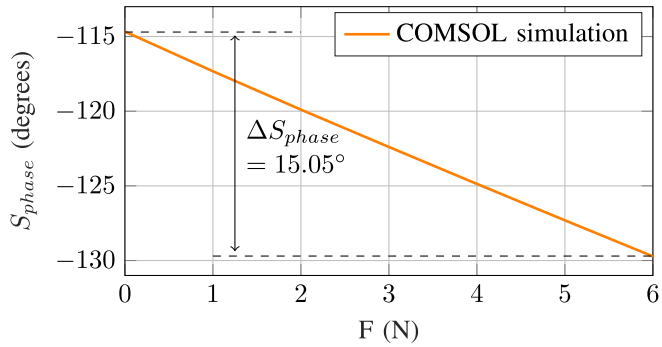

Fig. 4. COMSOL simulation results for our sensor with the selected design parameters. As the force applied to the sensor increases, the phase of the reflected wave, which travels along the signal trace of the sensor, decreases.

COMSOL Multiphysics to simultaneously capture the sensor's mechanical behavior — using the Solid Mechanics module — and the phase shift between a transmitted and reflected wave — using the RF module. Details on both components, as well as details on our design parameter selection, are given below.

Mechanical Component: Ecoflex 00–30 was selected for the dielectric polymer layer due to its ability to deform under applied loads while not yielding or fracturing under the mechanical stress level experienced. In order to simulate the non-linear hyperelastic mechanical behavior of Ecoflex 00–30, the Yeoh model was used with $C_1 = 17$ kPa, $C_2 = -0.2$ kPa, $C_3 = 0.023$ kPa [23]. The Ecoflex 00–30 was considered to be nearly incompressible and the initial bulk modulus used in our simulations was calculated using the relationship $K = \frac{E}{3(1-2\nu)}$, with a Young's modulus $E = 125$ kPa [24], and a Poisson's ratio $\nu = 0.49$. In order to provide a support and connection interface for our sensor prototypes for validation purposes, we mounted them onto a PCB transmission line that was integrated into our simulation. We note that such a PCB can be made smaller and flexible in future versions in order to increase the compactness of the overall sensor and to ease the integration with surgical robots.

RF Component: In order to simulate the wave backscattering capabilities of the sensor, we must excite it at a given RF frequency and observe the phase of the reflected signal. We choose a frequency of 900 MHz among the possible sub-1 GHz frequency bands because it has been widely used for in-vivo wireless backscatter sensing and has been shown to work robustly even when the signals go through multiple tissue layers [21]. The PCB was selected to have a standard 50 Ω impedance and implements a 900 MHz matched microstrip line. The top copper layer of the sensor is connected to the ground trace of the PCB with a 20 μm diameter tungsten wire, and the bottom copper layer of the sensor is placed directly onto the signal trace of the PCB, as illustrated in Fig. 3.

Electromagnetic waves propagate along the signal trace, visible in Fig. 3. Once they reach the sensor, they are reflected and travel back along the signal trace. These signal reflections are typically characterized by the reflection scattering parameter, S_{11}. The magnitude, $S_{mag} = |S_{11}|$, of the signal must lie between 0 and -1 dB to ensure that the majority of the input wave is backscattered. The phase, $S_{phase} = \angle(S_{11})$, is used as our main metric to evaluate the sensor performance across the various sensor designs assessed. Indeed, a large phase shift over the range of applied forces leads to a higher sensitivity and resolution of the applied force magnitude estimation.

Parameter Selection: Once both the mechanical and RF components of the sensor are fully set up, the final step is to solve for a set of design parameters that will result in sufficient phase change over the force range required for the particular application. We start here by designing a sensor applicable to a wide range of surgical procedures. Given that the mean of the average of measured forces has been reported to range from 0.04 N to 5.70 N for different surgical specialties — including ophthalmology, vascular surgery, neurosurgery, cardiothoracic surgery, general surgery, and urologic surgery [7], [25] — we selected to design our proposed sensor for use within this general range.

To understand the effects of varying each design parameter on the sensor performance, a range and step size was first selected for each parameter as follows: the thickness of copper and Ecoflex 00–30 layers were increased from 0.1 mm to 0.5 mm with a step size of 0.1 mm, and the width and length of the sensor were increased from 1 mm to 5 mm with a step size of 1 mm. Designs were then simulated under applied loads in the range of 0 N to 6 N with a step size of 1 N, resulting in the following general trends between the design parameters and scattering parameters. Overall, decreasing each design parameter resulted in minimal changes to the S_{mag} value, and all designs resulted in ranges of S_{mag} between 0 dB and -1 dB. In addition, decreasing each design parameter led to an increase in the range of S_{phase}. While maximizing this range of S_{phase} over the range of applied forces is desirable to enable higher sensitivity and resolution, the manual fabrication techniques used set a lower limit on the feasible design parameters. Therefore, the following set of values was chosen for the final sensor dimensions: 0.1 mm for the copper thickness, 0.2 mm for the Ecoflex 00–30 thickness, 2.0 mm for the sensor width, and 4.0 mm for the sensor length.

Simulation Results: Overall, this design showed a linear change in phase of 15.05° over 0 N to 6 N of force, as visible in Fig. 4. This full scale output would give the sensor a

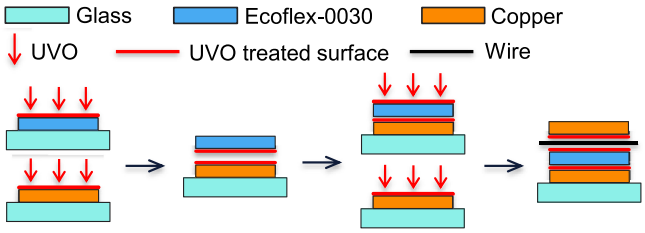

Fig. 5. Illustration of the fabrication steps for the sensor.

sensitivity of $2.51^\circ/\mathrm{N}$. The resolution of the sensor depends on the resolution of the testing equipment. In a wired setting with a 0.01° resolution VNA (Vector Network Analyzer, E5071 C Agilent Technologies), the sensor resolution would be 4 mN. Considering the wireless compatibility of the sensor, the sensor resolution would be 0.4 N in a wireless setting with 1° resolution as evaluated in our previous work [21]. Given that the sensor resolution should be at least one order of magnitude less than the force difference to be resolved (in order to reduce the effect of quantization error) [26], such sensor resolutions would be sufficient for surgical applications that require force measurements of 0.04 N to 6 N and 4 N to 6 N, respectively.

III. Sensor Fabrication

The sensors are then fabricated based on the final simulated design. The first step is to fabricate each component of the sensor, including the copper layers and the polymer layer. A DCH-355-3 Laser (Photonics Industries International, Inc.) was used to laser cut the 0.1 mm thick copper sheets into the desired dimensions (2 mm $\times$ 4 mm). To prepare the polymer layer, Ecoflex 00–30 part B was pre-mixed thoroughly for 30 seconds and then combined with a weight ratio of 1:1 with part A. After mixing for 3 minutes, the mixture was vacuum degassed at -1 Bar for 5 minutes. The mixture was then blade coated with a height of 0.2 mm on a glass slide. This polymer layer sat at room temperature for 4 hours and was then post-cured in 80 °C for an additional 2 hours to allow it to reach its maximum performance properties [27].

Once the components are prepared, the next step is to combine the layers to form the full sensor. In order to remove a variety of contaminants from surfaces and increase adhesion between the metal and polymer layers, every interface was UV/Ozone (UVO) treated for 60 seconds (UVO-Cleaner Model 42, Jelight Company, Inc.). As seen in Fig. 5, one side of a pre-cut copper piece and one side of the cured Ecoflex 00–30 were UVO treated. Ecoflex-0030 was then cut to meet the desired size specifications and placed onto the UVO-treated bottom copper layer with the UVO-treated surfaces facing each other. The other side of the Ecoflex 00–30 layer and the top copper layer were then UVO treated. Finally, a 8 mm long tungsten wire with a diameter of 20 μm was placed across the top of the Ecoflex 00–30, and the top copper layer was placed on top of the wire with the UVO-treated surface facing down. The fabricated sensor, shown from both the top (Fig. 6(a)) and side (Fig. 6(b)), was left to sit for 2 hours at room temperature to ensure a strong adhesion between the layers.

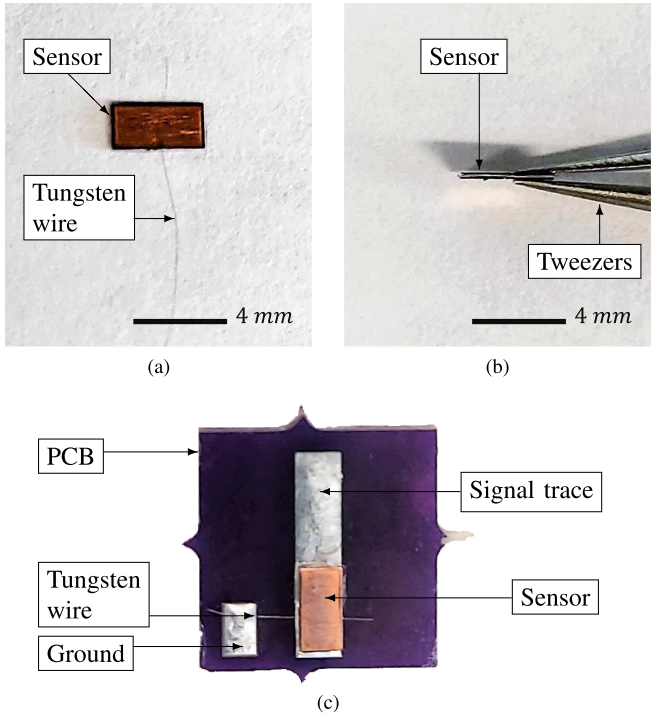

Fig. 6. Photos of the final fabricated sensors, with (a) a top view and (b) side view of one of the fabricated prototypes, and (c) a top view of the same prototype after assembly on the PCB.

The fabricated sensor was then mounted onto the PCB with the tungsten wire side facing up. Since the maximum use temperature of Ecoflex 00–30 is 232 °C [27], solder paste with a melting point of 219 °C [28] was used to prevent deformation of the polymer. The bottom copper layer was soldered onto the signal trace of the PCB and the tungsten wire to the ground trace. The sensor attached to the PCB is shown in Fig. 6(c).

IV. Sensor Evaluation

To evaluate the sensor performance and verify it matches the simulation results, we perform the following experiments.

A. Experimental Setup

The experimental setup shown in Fig. 7 was designed to enable known forces to be applied to the fabricated sensors and subsequently compared to the output from the sensors themselves. For this purpose, a linear actuator with an indenter is used to apply forces onto the sensor, which is mounted onto a load cell. The load cell, which provides the ground-truth measurements of the forces being applied, has a maximum measurable force of 49.5 N and an accuracy of 0.0098 N. The sensor itself is connected to a VNA that enables phase measurements in a wired configuration. We note that the Intermediate Frequency bandwidth of the VNA is set to 70 kHz, which is sufficient for measuring forces with a temporal resolution of 35 kHz.

It should also be noted that environmental factors should be considered since they could affect the mechanical behavior of the polymer [29], [30] and frequency response of the sensor [31].

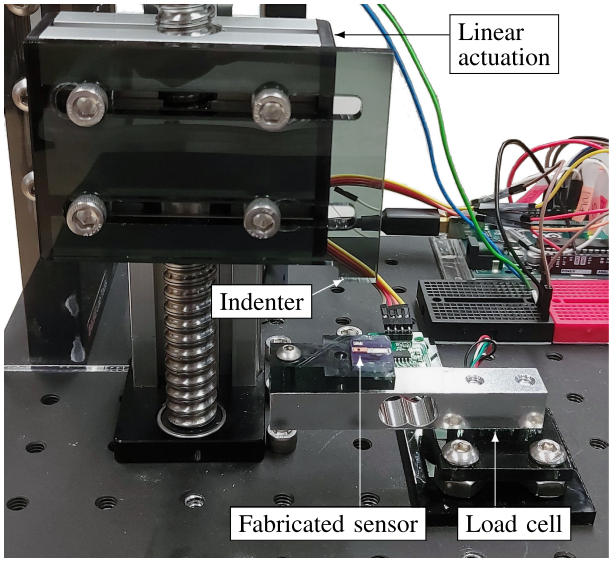

Fig. 7. Experimental setup used for the evaluation of the sensors.

Evaluations were performed under an average ambient room temperature of 22 °C and relative humidity of 50%. Since Ecoflex 00–30 has similar mechanical behavior for temperatures between 20 °C and 60 °C [32], the sensor is expected to show similar performance even when used inside the human body (typically 36.5 °C). And since the sensor will ultimately be hermetically sealed, such that external moisture will be prevented from coming in contact with the sensor, the effects of changes in humidity were not seen as a major concern. Further, since the electromagnetic fields generated by the human body typically have very low frequencies (few kHz [33]) compared to the 900 MHz working frequency of the sensor, it could be easily filtered out with the measuring equipment.

Finally, for filled silicone rubbers, including Ecoflex 00–30, it is found that stress softening (also known as the Mullins effect) occurs during cycles of loading and unloading paths [34]. It has been shown that in order to mitigate the effects of stress softening and obtain consistent mechanical properties, silicone rubbers should be pre-stretched for multiple cycles [35]. In addition, the stress softening increases progressively as the maximum stretch level rises [36]. Therefore, it was essential to pre-stretch the sensors for a number of cycles to obtain uniformity of the mechanical behavior. It was empirically found that the force-to-phase output of the sensor converges after 20 cycles. Therefore, every sensor was pre-conditioned with 20 initial cycles, with loads ranging from 0 N to 6 N, prior to data collection.

B. Experimental Results

Data for 10 loading cycles (trials 21-30) was collected for the two fabricated sensors. All trials are shown in purple in Fig. 8(a) and 8(b). We note that as the trial number increases, there is a slight decrease in phase, which can likely be attributed to the Mullins effect. However, the deviations are minimal, and it can be seen that across the range of applied loads, the measured phase remains relatively consistent from trial to trial. In addition, we

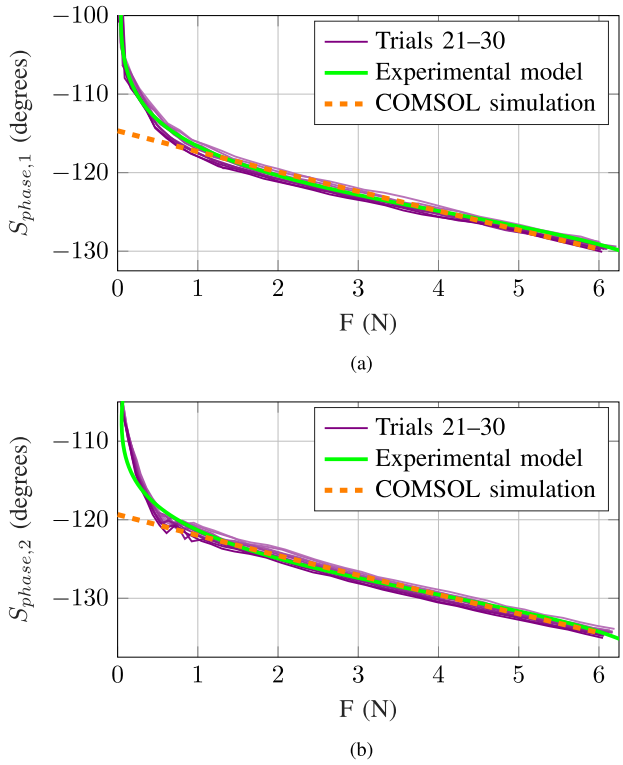

Fig. 8. Plots of the experimental results for trials 21 to 30, model created from the experimental data, and the results of the FEA for (a) sensor 1 and (b) sensor 2.

TABLE I
INTERPOLANT COEFFICIENTS OF THE EXPERIMENTAL MODEL FOR SENSOR 1 AND 2

Coefficients	p_1	p_2	p_3	q_1	q_2
$S_{phase,1}$	1.058	214.5	10910	257.2	16680
$S_{phase,2}$	1.465	317.4	17230	264.6	17670

TABLE II
SENSITIVITY AND RESOLUTION OF SENSOR 1 AND SENSOR 2

Force range and metric	0 - 0.5 N		0.5 - 6 N	
	Sensitivity	Resolution	Sensitivity	Resolution
Sensor 1	23.83 °/N	0.42 mN	2.88 °/N	3.47 mN
Sensor 2	19.82 °/N	0.5 mN	2.91 °/N	3.43 mN

note that even though there is an offset in phase between sensor 1 and sensor 2, the general shape and trend of the curves remain similar. The reason for this relative difference can be attributed to the accuracy of fabrication and integration of the sensor to the PCB, which includes several manual steps.

The experimental data was then compared to the FEA results presented in Section II. Since electromagnetic waves backscatter upon reaching the sensor on the PCB, the sensor position on the PCB signal trace affects the initial phase of the reflected wave at a steady state. Therefore, any slight error in sensor placement creates an offset compared to the simulation results. Therefore, the obtained phases from our physical prototypes were shifted, and an offset was added for comparison purposes. The results are visible in Fig. 8(a) and 8(b). It can be seen that in the force range

TABLE III
ROBOT CONFIGURATIONS SELECTED FOR THE DEMONSTRATION OF OUR FORCE SENSORS, WITH THE ESTIMATION OF THE FORCE USING OUR SENSOR MODEL, OVERLAID WITH THE GROUND TRUTH FORCE MEASUREMENT PROVIDED BY THE LOAD CELLS

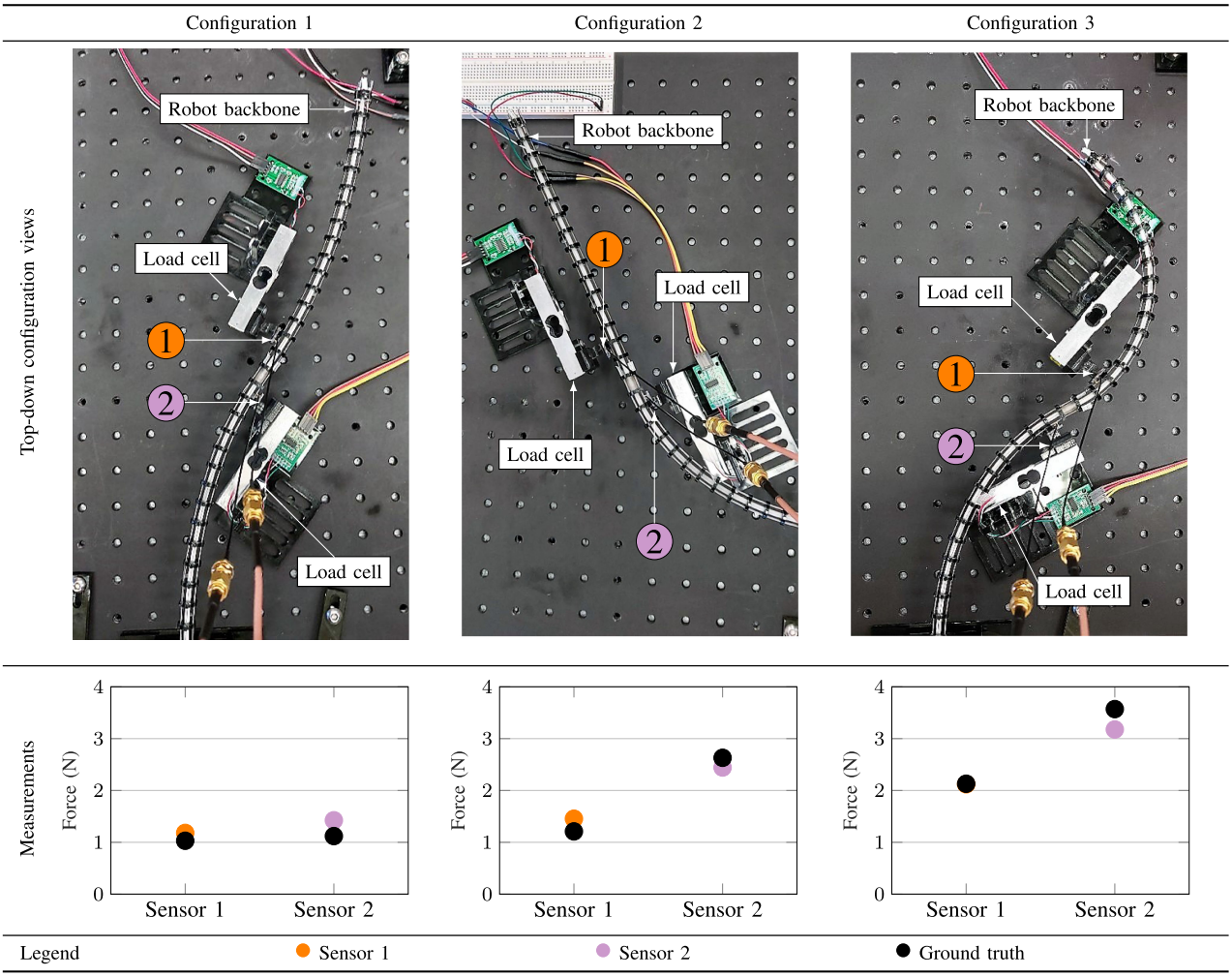

of 0 N to 0.5 N the FEA results differ from the experimental data. This difference can likely be explained by the presence of tiny gaps between the signal trace of the PCB and the bottom copper layer of the sensor, which were connected via a manual soldering process. If gaps exist, then the surface area of the sensor in contact changes as a force is applied until both surfaces are in full contact. This leads to a bigger change in sensor capacitance leading to an additional phase shift. However, in the range of 0.5 N to 6 N, it can be seen that the phase obtained using FEA overlaps well with the experimental data, with matching slopes. The comparison between the FEA results and the experimental data is satisfying and indicates that the FEA was successful in providing guidance for the sensor design in order to obtain the desired phase shift.

A model was then computed for each sensor to estimate the force for a measured phase. A 2^{nd} order rational was used and is given by,

$$F(S_{phase,i}) = \frac{p_1 S_{phase,i}^2 + p_2 S_{phase,i} + p_3}{S_{phase,i}^2 + q_1 S_{phase,i} + q_2}, \qquad (1)$$

where the coefficients used for each sensor are given in Table I. The sensor models are also shown in green in Fig. 8(a) and 8(b) and show a qualitatively good fit. The RMS errors between the experimental model and the experimental data is 0.16 N and 0.18 N for sensors 1 and 2, respectively. In addition, the full scale output of each sensor can be evaluated, and is found to be 27.77° and 25.93° for sensor 1 and sensor 2, respectively. Using the constructed sensor models, the sensitivity and resolution of each sensor can then be evaluated for the two main regions visible in Fig. 8(a) and Fig. 8(b) — forces below 0.5 N and forces above 0.5 N. As shown in Table II, the sensitivity and resolution for sensor 1 were 23.83°/N and 0.42 mN for 0–0.5 N, and 2.88 °/N and 3.47 mN for 0.5–6 N. The sensitivity and resolution for sensor 2 were 19.82°/N and 0.5 mN for 0–0.5 N, and 2.91°/N and 3.43 mN for 0.5–6 N. Overall, these resolutions are sufficient for many surgical applications [26].

It can be seen that the two sensors showed some slight differences in terms of RMS errors, full scale output, sensitivity, and resolution. These differences could be due to errors in the manual fabrication process, including errors in the dimensions of each layer or in the geometry of the sensor during their assembly.

In addition, due to possible imperfect parallelism between the indenter and the top surface of the sensor during evaluation, the applied force may not have been perfectly uniform or may have included shear components. These possible errors could be minimized with a more precise fabrication process and experimental setup in the future.

V. Demonstration

In this section, we propose a realistic use case for our sensor by attaching them to a tendon-driven robot. We then compare the estimated forces applied to the sensor, obtained using our previous model, against the ground truth provided by load cells placed along with the deployment environment.

A. Experimental Setup

A tendon-driven robot with a diameter of 12 mm was designed and fabricated for the demonstration. The robot is made of a flexible backbone and consists of two sections, each containing a set of 16 disks equally spaced 1 cm apart along the backbone. Two sets of 3 tendons are routed along the length of the backbone and used to actuate each segment. In order to attach a sensor to a disk along the length of the robot, a mount was designed, and the back side of the PCB was rigidly attached via adhesive to the mount. Each sensor was connected to a VNA port with a U.FL cable in order to both excite the sensor with a 900 MHz signal and to measure the phase shift induced by the deformation. For this demonstration, two sensors were mounted to the robot, one on each section, facing opposite directions. To assess the performance of the sensors in this more realistic use case, load cells were used as the designated environment 'obstacles,' and these measurements were used as the ground-truth forces. For three different robot configurations, the force sensors and environmental 'obstacles' interacted. For each sensor, 10 readings were collected and averaged for each of the three configurations. The models created in Section II were then used to calculate the force outputs from the sensors, and these values were compared to the ground-truth force readings from the load cells.

B. Results

The three different robot configurations for which the sensors were evaluated are visible in the first row of Table III. These shapes enabled forces of different magnitudes to be applied to our sensors, thus allowing us to validate our sensors across a wide force range. The estimated force magnitudes applied to the sensors are visible in the bottom row of Table III. The RMS error for sensor 1 and 2 across the three different robot configurations assessed are 0.17 N and 0.31 N, which is in accordance with the experimental model validated in Section II. The slightly higher RMS error shown by sensor 2 may have been due to non-uniform loading or shear forces, which are not considered when modeling the sensor. However, even with the current RMS error levels, the sensors have a high enough resolution and accuracy to provide multiple intermediate measurements between the upper and lower thresholds of applied forces during surgical operations, as seen by examining the required force ranges proposed for many different types of surgeries [25], [37], [38]. Thus, these results are satisfying and tend to show the performance and benefit of our proposed sensor in a more realistic use case.

VI. Conclusion

In this paper, we presented a new type of force sensor based on the principle of wave backscattering. This sensor transduces an applied force into a change in the phase of a reflected electromagnetic wave, thus enabling compatibility with wireless interfaces. The proposed sensor was simulated using FEA and designed to enable the measurement of forces in the range of 0 N to 6 N. Two prototypes were fabricated and evaluated experimentally and showed phase shifts following those expected from the simulations. A model was then created for each of the two fabricated sensors based on experimental data, with RMS error of 0.16 N and 0.18 N between the experimental data and the model for sensor 1 and 2, respectively. Finally, the performance of the sensors was evaluated in a realistic use case, where they were mounted on a continuum robot to measure contact forces with obstacles. The RMS error between the estimated forces and the ground truth measurements were 0.10 N and 0.33 N for sensor 1 and 2, respectively, which is in accordance with our modeling accuracy. Our next step will be to further miniaturize the sensor and the PCB. Miniaturizing the sensor is possible based on the analysis performed with our multiphysics model. Concerning the PCB, its dimensions were mainly chosen for implementation convenience and were not optimized. The PCB dimensions will therefore be reduced, and the PCB will be made flexible for better integration with robotic systems. The sensor will then be interfaced with Radio Frequency Integrated Circuit (RFIC) components in order to make it truly wireless. Because the sensor output is already encoded as a change in phase of a transmitted signal, it is immediately suitable for wireless usage without the need for additional electronics or wires to convert the output into a suitable format for wireless communication. This characteristic of our sensor makes it particularly well-suited for surgical applications where space within the lumen is a premium. We will also explore the integration of multiple sensors on a single flexible PCB that could be wrapped around the circumference of a robot, enabling high-density sensing.

References

[1] L. S. Gan, K. Zareinia, S. Lama, Y. Maddahi, F. W. Yang, and G. R. Sutherland, "Quantification of forces during a neurosurgical procedure: A pilot study," *World Neurosurgery*, vol. 84, no. 2, pp. 537–548, 2015.

[2] B. Bell *et al.*, "Integrating optical fiber force sensors into microforceps for orl microsurgery," in *Proc. Annu. Int. Conf. IEEE Eng. Med. Biol.*, 2010, pp. 1848–1851.

[3] D. C. Rucker and R. J. Webster, "Deflection-based force sensing for continuum robots: A probabilistic approach," in *Proc. IEEE/RSJ Int. Conf. Intell. Robots Syst.*, 2011, pp. 3764–3769.

[4] J. Konstantinova, A. Jiang, K. Althoefer, P. Dasgupta, and T. Nanayakkara, "Implementation of tactile sensing for palpation in robot-assisted minimally invasive surgery: A review," *IEEE Sensors J.*, vol. 14, no. 8, pp. 2490–2501, Aug. 2014.

[5] Y. Al-Handarish *et al.*, "A survey of tactile-sensing systems and their applications in biomedical engineering," *Adv. Mater. Sci. Eng.*, vol. 2020, pp. 1–17, 2020.

[6] M. I. Tiwana, S. J. Redmond, and N. H. Lovell, "A review of tactile sensing technologies with applications in biomedical engineering," *Sensors Actuators A: Phys.*, vol. 179, pp. 17–31, 2012.

[7] A. K. Golahmadi, D. Z. Khan, G. P. Mylonas, and H. J. Marcus, "Tool-tissue forces in surgery: A systematic review," *Ann. Med. Surg.*, vol. 65, 2021, Art. no. 102268.

[8] R. Peña, M. J. Smith, N. P. Ontiveros, F. L. Hammond, and R. J. Wood, "Printing strain gauges on intuitive surgical da vinci robot end effectors," in *Proc. IEEE/RSJ Int. Conf. Intell. Robots Syst.*, 2018, pp. 806–812.

[9] B. Gil, B. Li, A. Gao, and G.-Z. Yang, "Miniaturized piezo force sensor for a medical catheter and implantable device," *ACS Appl. Electron. Mater.*, vol. 2, no. 8, pp. 2669–2677, 2020.

[10] J. Heijmans, L. Cheng, and F. Wieringa, "Optical fiber sensors for medical applications–practical engineering considerations," in *Proc. 4th Eur. Conf. Int. Federation Med. Biol. Eng.*, 2009, pp. 2330–2334.

[11] D. Murzin *et al.*, "Ultrasensitive magnetic field sensors for biomedical applications," *Sensors*, vol. 20, no. 6, 2020, Art. no. 1569.

[12] H. Böse and E. Fuß, "Novel dielectric elastomer sensors for compression load detection," in *Electroactive Polymer Actuators and Devices (EAPAD)*, vol. 9056, Bellingham, Washington, USA: SPIE, 2014, pp. 232–244.

[13] K. Oliver-Butler, J. Till, and C. Rucker, "Continuum robot stiffness under external loads and prescribed tendon displacements," *IEEE Trans. Robot.*, vol. 35, no. 2, pp. 403–419, Apr. 2019.

[14] C. Shi *et al.*, "Shape sensing techniques for continuum robots in minimally invasive surgery: A survey," *IEEE Trans. Biomed. Eng.*, vol. 64, no. 8, pp. 1665–1678, Aug. 2017.

[15] Q. Qiao, G. Borghesan, J. De Schutter, and E. Vander Poorten, "Force from shape–estimating the location and magnitude of the external force on flexible instruments," *IEEE Trans. Robot.*, vol. 37, no. 5, pp. 1826–1833, Oct. 2021.

[16] T. Chen *et al.*, "Novel, flexible, and ultrathin pressure feedback sensor for miniaturized intraventricular neurosurgery robotic tools," *IEEE Trans. Ind. Electron.*, vol. 68, no. 5, pp. 4415–4425, May 2021.

[17] A. J. DeRouin *et al.*, "A wireless inductive-capacitive resonant circuit sensor array for force monitoring," *J. Sensor Technol.*, vol. 3, no. 3, pp. 63–69, 2013.

[18] H. Li *et al.*, "A miniature layered saw contact stress sensor for operation in cramped metallic slits," *Instruments Exp. Techn.*, vol. 61, no. 4, pp. 610–617, 2018.

[19] X. Yi, T. Wu, Y. Wang, R. T. Leon, M. M. Tentzeris, and G. Lantz, "Passive wireless smart-skin sensor using RFID-based folded patch antennas," *Int. J. Smart Nano Mater.*, vol. 2, no. 1, pp. 22–38, 2011.

[20] C. Girerd, Q. Zhang, A. Gupta, M. Dunna, D. Bharadia, and T. K. Morimoto, "Towards a wireless force sensor based on wave backscattering for medical applications," *IEEE Sensors J.*, vol. 21, no. 7, pp. 8903–8915, Apr. 2021.

[21] A. Gupta *et al.*, "WiForce: Wireless sensing and localization of contact forces on a space continuum," in *Proc. 18th USENIX Symp. Netw. Syst. Des. Implementation. USENIX Assoc.*, 2021, pp. 827–844. [Online]. Available: https://www.usenix.org/conference/nsdi21/presentation/gupta

[22] Y. Ma, Z. Luo, C. Steiger, G. Traverso, and F. Adib, "Enabling deep-tissue networking for miniature medical devices," in *Proc. Conf. ACM Special Int. Group Data Commun.*, 2018, pp. 417–431.

[23] D. Steck, J. Qu, S. B. Kordmahale, D. Tscharnuter, A. Muliana, and J. Kameoka, "Mechanical responses of ecoflex silicone rubber: Compressible and incompressible behaviors," *J. Appl. Polym. Sci.*, vol. 136, no. 5, 2019, Art. no. 47025.

[24] Y.-L. Park, C. Majidi, R. Kramer, P. Bérard, and R. J. Wood, "Hyperelastic pressure sensing with a liquid-embedded elastomer," *J. Micromechanics Microengineering*, vol. 20, no. 12, 2010, Art. no. 125029.

[25] B. K. Canales, D. Weiland, S. Reardon, and M. Monga, "Urethral catheter insertion forces: A comparison of experience and training," *Int. Braz J.*, vol. 35, pp. 84–89, 2009.

[26] G. L. McCreery, A. L. Trejos, M. D. Naish, R. V. Patel, and R. A. Malthaner, "Feasibility of locating tumours in lung via kinaesthetic feedback," *Int. J. Med. Robot. Comput. Assist. Surg.*, vol. 4, no. 1, pp. 58–68, 2008.

[27] E. Series, "Smooth-on, inc." 2013. [Online]. Available: https://www.smooth-on.com/tb/files/ECOFLEX_SERIES_TB.pdf

[28] M. Chemicals, "Safety data sheet," 2017. [Online]. Available: https://assets.testequity.com/te1/Documents/pdf/mg-sds-4902p.pdf

[29] J. M. L. D. Reis, "Effect of temperature on the mechanical properties of polymer mortars," *Mater. Res.*, vol. 15, no. 4, pp. 645–649, 2012.

[30] G. Zheng, Y. Kang, J. Sheng, Q. Qin, H. Wang, and D. Fu, "Influence of moisture content and time on the mechanical behavior of polymer material," *Sci. China Ser. E: Technological*, vol. 47, no. 5, pp. 595–607, 2004.

[31] F. Abdollahi-Mamoudan, S. Savard, C. Ibarra-Castanedo, T. Filleter, and X. Maldague, "Influence of different design parameters on a coplanar capacitive sensor performance," *NDT E. Int.*, vol. 126, 2022, Art. no. 102588.

[32] Z. Liao, M. Hossain, X. Yao, R. Navaratne, and G. Chagnon, "A comprehensive thermo-viscoelastic experimental investigation of ecoflex polymer," *Polym. Testing*, vol. 86, 2020, Art. no. 106478.

[33] J. Couto and W. M. Grill, "Kilohertz frequency deep brain stimulation is ineffective at regularizing the firing of model thalamic neurons," *Front. Comput. Neurosci.*, vol. 10, 2016, Art. no. 22.

[34] R. Ogden and D. Roxburgh, "A pseudo-elastic model for the mullins effect in filled rubber," *Proc. Math. Phys. Eng. Sci.*, vol. 455, pp. 2861–2877, 1988.

[35] X. Lv, L. Liu, Y. Liu, and J. Leng, "Electromechanical modeling of softening behavior for dielectric elastomers," *J. Appl. Mechanics*, vol. 85, no. 11, 2018, Art. no. 111010.

[36] J. Diani, B. Fayolle, and P. Gilormini, "A review on the mullins effect," *Eur. Polym. J.*, vol. 45, no. 3, pp. 601–612, 2009.

[37] R. N. Pedro, D. Weiland, S. Reardon, and M. Monga, "Ureteral access sheath insertion forces: Implications for design and training," *Urological Res.*, vol. 35, no. 2, pp. 107–109, 2007.

[38] J. Peirs *et al.*, "A micro optical force sensor for force feedback during minimally invasive robotic surgery," *Sensors Actuators A: Phys.*, vol. 115, no. 2–3, pp. 447–455, 2004.